

**AFRL-ML-WP-TP-2006-463**

**MICROSTRUCTURAL  
CHARACTERIZATION AND  
MODELING OF DISCONTINUOUSLY-  
REINFORCED ALUMINUM  
COMPOSITES (POSTPRINT)**



**Jonathan E. Spowart**

**AUGUST 2006**

**Approved for public release; distribution is unlimited.**

**STINFO COPY**

**This is a work of the United States Government and is not subject to copyright protection  
in the United States.**

**MATERIALS AND MANUFACTURING DIRECTORATE  
AIR FORCE RESEARCH LABORATORY  
AIR FORCE MATERIEL COMMAND  
WRIGHT-PATTERSON AIR FORCE BASE, OH 45433-7750**

<b>REPORT DOCUMENTATION PAGE</b>					<i>Form Approved</i> OMB No. 0704-0188	
The public reporting burden for this collection of information is estimated to average 1 hour per response, including the time for reviewing instructions, searching existing data sources, gathering and maintaining the data needed, and completing and reviewing the collection of information. Send comments regarding this burden estimate or any other aspect of this collection of information, including suggestions for reducing this burden, to Department of Defense, Washington Headquarters Services, Directorate for Information Operations and Reports (0704-0188), 1215 Jefferson Davis Highway, Suite 1204, Arlington, VA 22202-4302. Respondents should be aware that notwithstanding any other provision of law, no person shall be subject to any penalty for failing to comply with a collection of information if it does not display a currently valid OMB control number. <b>PLEASE DO NOT RETURN YOUR FORM TO THE ABOVE ADDRESS.</b>						
<b>1. REPORT DATE (DD-MM-YY)</b> August 2006		<b>2. REPORT TYPE</b> Journal Article Postprint		<b>3. DATES COVERED (From - To)</b>		
<b>4. TITLE AND SUBTITLE</b> MICROSTRUCTURAL CHARACTERIZATION AND MODELING OF DISCONTINUOUSLY-REINFORCED ALUMINUM COMPOSITES (POSTPRINT)				<b>5a. CONTRACT NUMBER</b> In-house		
				<b>5b. GRANT NUMBER</b>		
				<b>5c. PROGRAM ELEMENT NUMBER</b> N/A		
<b>6. AUTHOR(S)</b> Jonathan E. Spowart				<b>5d. PROJECT NUMBER</b> M02R		
				<b>5e. TASK NUMBER</b> 40		
				<b>5f. WORK UNIT NUMBER</b> 00		
<b>7. PERFORMING ORGANIZATION NAME(S) AND ADDRESS(ES)</b>  Metals Branch/Metals Development Team (AFRL/MLLMD) Metals, Ceramics & Nondestructive Evaluation Division Materials and Manufacturing Directorate Air Force Research Laboratory, Air Force Materiel Command Wright-Patterson AFB, OH 45433-7750				<b>8. PERFORMING ORGANIZATION REPORT NUMBER</b>  AFRL-ML-WP-TP-2006-463		
<b>9. SPONSORING/MONITORING AGENCY NAME(S) AND ADDRESS(ES)</b>  Materials and Manufacturing Directorate Air Force Research Laboratory Air Force Materiel Command Wright-Patterson AFB, OH 45433-7750				<b>10. SPONSORING/MONITORING AGENCY ACRONYM(S)</b> AFRL-ML-WP		
				<b>11. SPONSORING/MONITORING AGENCY REPORT NUMBER(S)</b> AFRL-ML-WP-TP-2006-463		
<b>12. DISTRIBUTION/AVAILABILITY STATEMENT</b> Approved for public release; distribution is unlimited.						
<b>13. SUPPLEMENTARY NOTES</b> Journal article postprint published in <i>Materials Science and Engineering A</i> , Vol. 425 (2006) by Elsevier B.V. This is a work of the United States Government and is not subject to copyright protection in the United States. PAO Case Number: AFRL/WS 05-0182, 3 Feb 2005.						
<b>14. ABSTRACT</b> Models for predicting the constitutive behavior of spatially-heterogeneous microstructures such as discontinuously-reinforced aluminum (DRA) and other metallic matrix composites based on unit cell approaches generally do not incorporate higher-order microstructural features such as degree of homogeneity and spatial anisotropy of the reinforcement phase. Moreover, more complex numerical models rarely encompass the volumes of material necessary to ensure statistical relevance. The present contribution offers an alternative approach for quantifying and then incorporating the microstructural homogeneity of these materials within an elastic-plastic finite element code. An attempt is made to model both the micromechanical length scale associated with the individual reinforcement particles and the microstructural length scale associated with their spatial distribution, at a greatly-reduced computational expense, by using a volume-averaged, discretized approach.						
<b>15. SUBJECT TERMS</b> Discontinuously-reinforced aluminum, spatial heterogeneity, micro-mechanical modeling, microstructure-property relationships						
<b>16. SECURITY CLASSIFICATION OF:</b>			<b>17. LIMITATION OF ABSTRACT:</b> SAR	<b>18. NUMBER OF PAGES</b> 20	<b>19a. NAME OF RESPONSIBLE PERSON (Monitor)</b> Jonathan E. Spowart <b>19b. TELEPHONE NUMBER (Include Area Code)</b> N/A	
<b>a. REPORT</b> Unclassified	<b>b. ABSTRACT</b> Unclassified	<b>c. THIS PAGE</b> Unclassified				

# Microstructural characterization and modeling of discontinuously-reinforced aluminum composites

Jonathan E. Spowart\*

*Air Force Research Laboratory, Materials and Manufacturing Directorate, Wright-Patterson Air Force Base, OH 45433, USA*

Received 14 September 2005; received in revised form 3 March 2006; accepted 20 March 2006

## Abstract

Models for predicting the constitutive behavior of spatially-heterogeneous microstructures such as discontinuously-reinforced aluminum (DRA) and other metallic matrix composites based on unit cell approaches generally do not incorporate higher-order microstructural features such as degree of homogeneity and spatial anisotropy of the reinforcement phase. Moreover, more complex numerical models rarely encompass the volumes of material necessary to ensure statistical relevance. The present contribution offers an alternative approach for quantifying and then incorporating the microstructural homogeneity of these materials within an elastic-plastic finite element code. An attempt is made to model both the *micromechanical* length scale associated with the individual reinforcement particles and the *microstructural* length scale associated with their spatial distribution, at a greatly-reduced computational expense, by using a volume-averaged, discretized approach. A key assumption in this approach is that below the length scale of the discretization, the microstructure can be modeled by a uniform array of reinforcement particles. The effect of the level of discretization on predictions of microstructure-property relationships are not addressed directly in the present work. Detailed comparisons of the present model with discretely-modeled matrix-particle geometries will therefore form the basis of a subsequent publication. Nevertheless, several microstructure-property relationships are developed which reveal empirical relationships between microstructural homogeneity and the elastic-plastic response.

Published by Elsevier B.V.

**Keywords:** Discontinuously-reinforced aluminum; Spatial heterogeneity; Micro-mechanical modeling; Microstructure-property relationships

## 1. Introduction

Microstructural details such as degree of homogeneity and spatial anisotropy of the reinforcement phase can have a profound effect on the mechanical properties of spatially-heterogeneous microstructures such as discontinuously-reinforced aluminum (DRA) and other metallic matrix composites [1–6]. A number of previous attempts have been made to incorporate different levels of microstructural detail into material property models for discontinuously-reinforced composite materials [2,7–21]. As computational power has continued to increase, numerically-based 2D and 3D finite element methods have become increasingly common. Over the last 15 years, there has also been a progression in size and complexity of the models; from the early periodic unit cell models of Christman et al. [17] and Tvergaard [21] through to more recent work

on 2D [11,22–25] and 3D [15,18,22,26,27] elastic-plastic analyses using multi-particle models, including the most recent microstructure-based approaches [8,9,11,18,23–25]. For example, Chawla et al. [18] used manual serial-sectioning to produce a microstructurally accurate 3D model of a 2080/SiC/20p aluminum composite containing 14 SiC particles. In order to faithfully reproduce the individual particle morphologies, a total of 76,000 elements was required. Other multi-particle models typically contain between 10 and 100 particles and require around  $10^4$ – $10^5$  elements. If this is extrapolated to the numbers of particles needed to statistically represent microstructural heterogeneities that operate on much larger length scales, e.g. particle clustering, then these “brute force” approaches to finite element analysis quickly approach the practical limit of current computational capabilities. For example, microstructural heterogeneities in DRA have been reported on the scale of several millimeters [1,28]. In order to model the  $10^5$ – $10^6$  particles contained in a 1 mm cube of such a material, a brute force approach would require  $10^8$ – $10^9$  elements, clearly beyond the limit of current computational capabilities.

\* Tel.: +1 937 255 1340; fax: +1 937 255 3007.

E-mail address: jonathan.spowart@wpafb.af.mil.

The present work therefore represents a departure from the previous approaches, in that it attempts to reduce the complexity and size of the overall model by developing a generic framework both to quantify the spatial homogeneity and then to directly model the influence of spatial homogeneity on mechanical properties, using a finite element scheme coupled with micromechanical (analytical) modeling. The approach is computationally inexpensive, and therefore is capable of modeling significant amounts of material, in either 2D or 3D. Microstructural details such as clustering and/or homogeneity can be incorporated into this modeling scheme without resorting to unrealistic approximations such as periodic boundary conditions [15,26] or artificial symmetry bounds [11,27]. The ability to quantify and incorporate statistical variations in reinforcement volume fraction (i.e. spatial homogeneity) into models for mechanical behavior is seen as a significant step forward in the ongoing effort to understand the effects of spatial homogeneity on mechanical performance of extruded DRA materials.

## 2. Quantifying spatial homogeneity using the MSAAF technique

The present work concentrates on predicting the elastic and small-strain plastic response of DRA microstructures that display varying levels of spatial homogeneity, due to differences in their processing histories. The Multi-Scalar Analysis of Area Fractions (MSAAF) technique, originally developed by Spowart et al. [29], is used to quantify the spatial homogeneity of the different DRA microstructures by dividing up the microstructure into local grid squares and then measuring the coefficient of variation of local area fractions on a sectioning plane,  $CV(A_f) = \sigma_{A_f}/A_f$ , where  $\sigma_{A_f}$  is the standard deviation of the individual local area fractions on the plane and  $A_f$  is their statistical mean. For a microstructure comprising a Poisson random distribution of mono-sized circular particles of diameter  $d_p$ , the statistical parameter should vary with grid size,  $Q$ , according to Eq. (1) for  $Q \gg d_p$

$$CV(A_f) = \left( \frac{\pi}{4A_f} \right)^{0.5} \left( \frac{Q}{d_p} \right)^{-1} \quad (1)$$

For  $Q < d_p$ , however, it is found that  $CV(A_f)$  depends only on the mean area fraction of the original image, regardless of the spatial distribution of particles. In this case, Eq. (2) is more appropriate

$$CV(A_f)|_{\lim Q/d_p \rightarrow 0} = \left( \frac{1 - A_f}{A_f} \right)^{0.5} \quad (2)$$

Fig. 1 shows MSAAF data obtained from a model microstructure generated using the RSA algorithm [29] comprising 10,000 randomly-distributed non-overlapping mono-sized disks with an overall area fraction of  $A_f = 0.022$ . There is excellent agreement between the calculated values of  $CV(A_f)$  and the predictions of Eqs. (1) and (2) for an equivalent Poisson random distribution of points. The slope of the straight-line portion on this log–log plot is close to  $-1.0$ , due to the random nature of the microstructure. The technique provides microstructural information over many length scales, from roughly the particle size

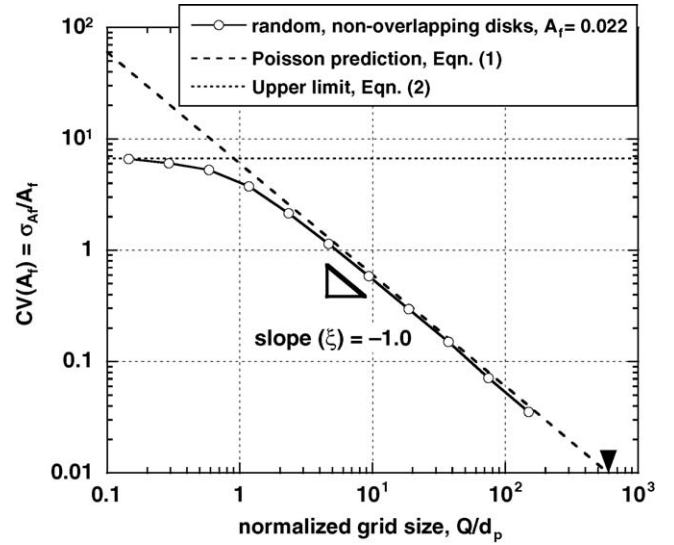


Fig. 1. MSAAF results showing variation of  $CV(A_f)$  with normalized length scale,  $Q/d_p$  for random, non-overlapping mono-sized disks with overall  $A_f = 0.022$ . Also plotted are lines representing Eqs. (1) and (2) for the equivalent Poisson random distribution. The small black triangle on the lower right horizontal axis represents the 1% homogeneous length scale,  $L_H^{0.1} = 580 d_p$ .

upwards, however, it is often convenient to characterize the level of spatial heterogeneity in the microstructure by assigning a single scalar parameter, the *Homogeneous Length Scale* or  $L_H$ . This parameter (with units of length) represents the microstructural length scale beyond which the microstructure is homogeneous to within a prescribed range. For example, one may define the parameter  $L_H^{0.01}$  as the length scale beyond which the local statistical variation in area fraction is no greater than 1%, indicated by the triangular symbol in Fig. 1. For this microstructure of non-overlapping circular discs with an overall area fraction of 0.022,  $L_H^{0.01} = 580 \times d_p$ , where  $d_p$  is the diameter of the (mono-sized) particles, however, for experimental microstructures  $L_H^{0.01}$  is typically measured in  $\mu\text{m}$  or  $\text{mm}$ . When comparing different microstructures with similar area fractions, the smaller the homogeneous length scale, the more homogeneous (or less clustered) the microstructure. Alternatively, one may consider the slope,  $\varepsilon$  as an indicator of microstructural heterogeneity. Steeper slopes (i.e. more negative) suggest more uniform microstructures, whereas shallower slopes (i.e. less negative) suggest more clustered or heterogeneous microstructures. Generally, this is a less sensitive descriptor of homogeneity than  $L_H$ .

### 2.1. Extension of MSAAF for anisotropic microstructures

It was anticipated that extrusion of the DRA would lead to microstructural anisotropy in the longitudinal plane. In order to include microstructural anisotropy in the measurement of spatial homogeneity, the original MSAAF technique was modified to allow for *anisotropic* resampling. Instead of using isotropic resampling, whereby pixels in the new image replace square arrays of pixels in the original image (i.e.  $1 \times 1$ ,  $2 \times 2$ ,  $4 \times 4$ , etc.) anisotropic resampling is used, where single pixels replace *strips* of pixels in the original image, i.e.  $1 \times 2$ ,

$1 \times 4$ ,  $1 \times 8$ , etc. for strips oriented horizontally on the image (parallel to the extrusion direction), and  $2 \times 1$ ,  $4 \times 1$ ,  $8 \times 1$ , etc. for strips oriented vertically (transverse to the extrusion direction).

The anisotropic analysis using oriented pixel *strips* enables differentiation between the two orthogonal directions in the image. The means and standard deviations of all the gray-levels in each strip are calculated as for the isotropic case, but are now used to compute two separate coefficients of variation,  $CV_1$  for horizontal strips and  $CV_2$  for vertical strips. This allows two different MSAAF curves to be plotted, and leads to the definition of two separate (in-plane) homogeneous length scale parameters,  $L_{H1}$  and  $L_{H2}$ . For randomly-distributed non-overlapping mono-sized disks, the slopes of the anisotropic MSAAF curves will be close to  $-0.5$  (cf.  $-1.0$  for the isotropic case) which makes extrapolation of the straight-line portion of the curve to a CV of 0.01 somewhat impractical. For this reason,  $L_H$  is typically defined at a CV of 10% (i.e.  $L_{H1}^{0.1}$  and  $L_{H2}^{0.1}$ ) for anisotropic microstructures such as these. In addition, the ratio of the two homogeneous length scales is a measure of the amount of anisotropy in the microstructure, and is therefore another microstructural descriptor which may be related to processing conditions (see Section 3).

### 3. Experimental

Spherical, gas-atomized matrix alloy powders of nominal composition Al-0.27 Cu-0.26 Fe-0.97 Mg-0.56 Si (wt.%, 6061 aluminum alloy) were classified into three powder lots with average particle sizes of 26.4, 42.0 and 108.6  $\mu\text{m}$ . These powders were then blended with high purity F600 grade SiC (average particle size 13.4  $\mu\text{m}$ ) to produce three different composite materials with increasing levels of spatial heterogeneity, as the particle size ratio (PSR) is increased from 2:1 to 3:1 to 8:1 [1]. Fig. 2 shows optical micrographs of longitudinal sections through typical composite microstructures for each of the three different materials.

Five separate regions were carefully selected from each longitudinally-sectioned DRA microstructure, in order to provide adequate statistics for the measurement of spatial homogeneity, and also to ensure that several duplicate images with the same overall area fraction were available for numerical modeling. The area of each image was  $667 \mu\text{m} \times 667 \mu\text{m}$ , and the mean area fraction of the images was measured as  $0.275 \pm 0.003$ . Additionally, particle aspect ratios in the longitudinal section plane were measured using quantitative image analysis software (Image Processing Toolkit, version 3.0) [30]. The average aspect ratio of the F-600 grade SiC particles,  $s$ , was calculated to be 2.0.

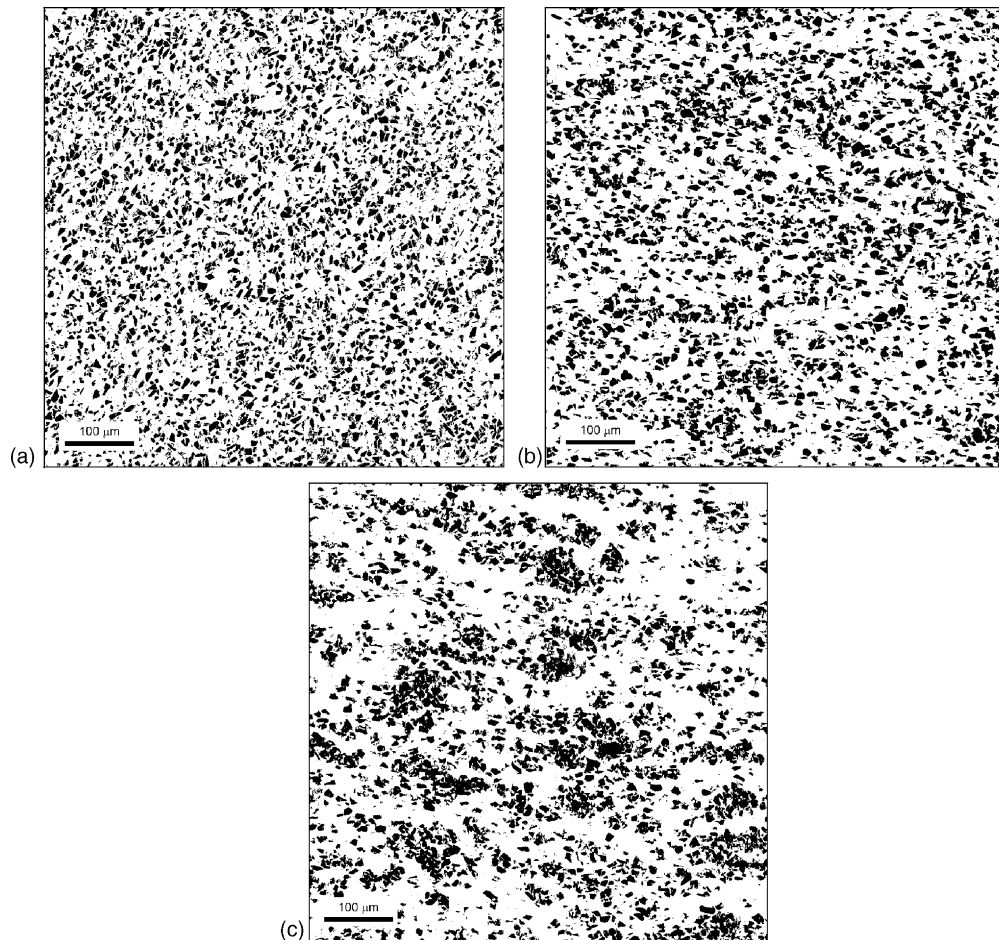


Fig. 2. Optical micrographs showing longitudinal sections through extruded DRA composites: (a) PSR = 2:1, (b) PSR = 3:1, (c) PSR = 8:1. Extrusion direction is horizontal. Note decreasing spatial homogeneity and increasing microstructural anisotropy with increasing PSR.



#### 4. Modeling of composite mechanical response

A combined model was developed to describe the effects of microstructure on the composite mechanical response for the different DRA materials. Composite behavior at the length scale of the reinforcement particles was modeled using a micromechanical approach based on the Eshelby equivalent inclusion method [31,32] for predicting the elastic and small-strain plastic response of idealized two-phase materials containing ellipsoidal inclusions. The overall composite behavior was modeled using a finite element code to discretize the microstructure into individual domains which had constitutive properties given by the Eshelby model. The combined model thus contains both micromechanical details at shorter length scales and microstructural information at longer length scales, thereby providing a fairly efficient framework for modeling the different spatial distributions of the reinforcement particles without requiring the level of complexity associated with a brute force meshing approach.

##### 4.1. Micromechanical modeling using the Eshelby equivalent inclusion method

The Eshelby equivalent inclusion method is a technique whereby the elastic behavior (and to a limited extent, the plastic behavior) of a two-phase material containing ellipsoidal inclusions can be predicted, based on the calculation of internal stresses that arise due to a generalized *misfit strain* between the shapes of the two constituent phases, matrix and inclusion.<sup>1</sup> For example, during elastic loading, the misfit may arise due to a stiffer inclusion wishing to deform to a lesser extent than a more compliant matrix material under the same applied load, whereas during plastic straining, the misfit might arise due to plastic deformation of the matrix whilst the inclusion remains elastic. The Eshelby analysis shows that for a generalized misfit strain,  $\varepsilon^{*T}$ , the internal stress within an ellipsoidal inclusion,  $\sigma_I$ , is given by [33]

$$\sigma_I = C_m(S - I)\{C_I - C_m\}^{-1}C_I\varepsilon^{*T} \quad (3)$$

Here  $C_m$  is the stiffness tensor of the matrix material,  $S$  the Eshelby tensor,  $I$  the identity matrix, and  $C_I$  is the stiffness tensor of the inclusion. In order to extend the Eshelby model to cope with non-dilute systems containing an inclusion volume fraction  $f$ , the mean-field approximations of Mori and Tanaka [34] and Pedersen [35] are used, whereby the volume-averaged stresses in each constituent phase,  $\langle\sigma\rangle_m$  and  $\langle\sigma\rangle_I$  can be given in terms of the equivalent transformation strain,  $\varepsilon^T$  as

$$\langle\sigma\rangle_m = -fC_m(S - I)\varepsilon^T \quad (4)$$

and

$$\langle\sigma\rangle_I = (1 - f)C_m(S - I)\varepsilon^T \quad (5)$$

<sup>1</sup> In what follows, the particles are referred to as *inclusions*, in keeping with Eshelby's original treatment.

The composite elastic stiffness tensor,  $C_c$ , can then be obtained directly from the constituent volume-averaged stresses,  $\langle\sigma\rangle_m$  and  $\langle\sigma\rangle_I$  as

$$C_c = [C_m^{-1} - f\{(C_I - C_m)[S - f(S - I)] - C_m\}^{-1} \\ (C_I - C_m)C_m^{-1}]^{-1} \quad (6)$$

A freely-available computer code [36] was used to evaluate this expression for  $C_c$  at volume fractions between 0 (pure matrix) and 1 (pure reinforcement) in order to provide material property data for input into the finite element model as engineering constants. Due to symmetry, the stiffness tensor for transversely-isotropic materials such as the extruded DRA composite reduces to seven independent components. Expressed in terms of engineering constants, these components are  $E_{11}$ ,  $E_{22} = E_{33}$ ,  $\nu_{12} = \nu_{13}$ ,  $\nu_{21} = \nu_{31}$ ,  $\nu_{23} = \nu_{32}$ ,  $G_{12} = G_{13}$  and  $G_{23} = G_{32}$ , where the one-direction is chosen to be parallel to the extrusion axis, and the (equivalent) two- and three-directions are transverse to the extrusion axis.

##### 4.1.1. Composite yield criterion

The Tresca or *maximum shear stress* yield criterion used for the composite can be generally stated as  $\Delta\sigma_{12} = 2k$ , where  $\Delta\sigma_{12}$  is the *maximum* deviatoric stress measured in the (1–2) plane, and  $k$  is the yield stress measured in pure shear. For uniaxial tension in the axial direction under an applied load  $\sigma^A$ ,  $\sigma_1 = \sigma^A$  and  $\sigma_2 = \sigma_3 = 0$ , therefore

$$\Delta\sigma_{12} = \sigma^A = \sigma_Y = 2k \quad (7)$$

For a transversely-isotropic material where the two- and three-axes are equivalent

$$\sigma_Y = (\bar{\sigma}_{1m} - \bar{\sigma}_{2m}) = (\bar{\sigma}_{1m} - \bar{\sigma}_{3m}) = \Delta\sigma_{12m} \quad (8)$$

Here  $\sigma_{Ym}$  is the matrix uniaxial yield stress and  $\bar{\sigma}_{1m}$ ,  $\bar{\sigma}_{2m}$ , and  $\bar{\sigma}_{3m}$  are given by the sum of the mean internal misfit stresses arising due to the stiffness mismatch between particle and matrix,  $\langle\sigma_i\rangle$ , and the appropriate component of the applied stress,  $\sigma_i^A$ . For uniaxial tension in the axial direction,  $\sigma_1^A > 0$ ,  $\sigma_2^A = \sigma_3^A = 0$ , therefore the composite yield criterion based on volume-averaged matrix stresses becomes

$$\sigma_{Y1c} = \sigma_{Ym} - (\langle\sigma_1\rangle_m - \langle\sigma_2\rangle_m) \quad (9)$$

The yield stress of the composite is higher than that of the matrix material since  $\langle\sigma_1\rangle_m < \langle\sigma_2\rangle_m$  for all particle aspect ratios  $>1$ . Furthermore, the matrix deviatoric stress ( $\Delta\sigma_{12m}$ ) will scale linearly [33] with the applied stress, i.e.  $\Delta\sigma_{12m} = P_1\sigma_1^A$ . The scalar parameter,  $P_1$ , effectively describes the difference in load partitioning between the axial and transverse directions in the composite, averaged over all the matrix volume. Accordingly, the yield criterion for the matrix (and hence the composite) can be written

$$\sigma_{Y1c} = \frac{\sigma_{Ym}}{P_1} \quad (10)$$

For the particle-reinforced composite system Al/SiC/27.5p,  $P_1$  evaluates to 0.724 for axial loading of inclusions with aspect ratio  $s=2$ , increasing the yield stress in the axial direction by

around 35%, compared to the un-reinforced matrix. Similar calculations can also be performed for transverse loading, however, due to the aspect ratios of the particles, load-sharing in the transverse direction is slightly less efficient than in the axial direction, therefore  $\sigma_{Y2c} = \sigma_{Y3c} < \sigma_{Y1c}$ . For the purposes of the present work, the yield surface is assumed to be an ellipsoid, with major axes given by  $\sigma_{Y1c}$ ,  $\sigma_{Y2c}$  and  $\sigma_{Y3c}$ .

#### 4.1.2. Composite strain-hardening behavior

This treatment is also applicable when the misfit strain arises as a result of matrix plasticity. With the assumption of perfectly-plastic deformation at constant volume and a uniaxial plastic strain of  $\varepsilon_{1m}^{pl}$ , the transformation strain for an isolated inclusion is given by

$$\varepsilon^{*T} = \begin{bmatrix} -\varepsilon_{1m}^{pl} \\ \frac{1}{2}\varepsilon_{1m}^{pl} \\ \frac{1}{2}\varepsilon_{1m}^{pl} \end{bmatrix} \quad (11)$$

This provides another matrix deviatoric stress term,  $\Delta\sigma_{12m}^{pl}$ , which depends linearly on the level of matrix plastic strain. Using the approximation  $\varepsilon_c^{pl} = (1 - f)\varepsilon_m^{pl}$  [33], it follows that  $\Delta\sigma_{12m}^{pl} = -W\varepsilon_c^{pl}$ , where  $\varepsilon_c^{pl}$  is the average plastic strain along the axial direction, and  $W$  has units of MPa/ $\mu\varepsilon$  (for Al/SiC/27.5p,  $W = 17.7$  GPa). With a perfectly-plastic matrix, linear strain-hardening is predicted for the composite, i.e.

$$\sigma_{Ym} = -W\varepsilon_c^{pl} + P\sigma^A \quad (12)$$

In this approximation, the only contribution to strain-hardening is from load partitioning between the elastic particles and the perfectly plastic matrix. However, any hardening (or softening) that may occur in the matrix during deformation will have additional effects. For example, parabolic work-hardening as often seen in aluminum alloys would dramatically increase the strain-hardening rate. Conversely, relaxation mechanisms such as interfacial debonding, cavitation [37], dislocation movement [38] and/or interfacial diffusion [39] can lower the overall strain-hardening rate. In an attempt to better predict the initial strain-hardening response of the composite, an additional (matrix) strain-hardening term which accounts for the initial work-hardening of the 6061 aluminum alloy matrix is included in Eq. (12), to give an overall strain-hardening rate of

$$\frac{d\sigma}{d\varepsilon_c^{pl}} = \frac{W}{P} + \frac{d\sigma}{d\varepsilon_m^{pl}} \quad (13)$$

Fig. 3 shows the predicted elastic-plastic responses for three different reinforcement volume fractions of aligned ( $s = 2.0$ ) particles, using the following handbook data [33,40] for the matrix and reinforcement constituent properties:  $E_{Al} = 70$  GPa,  $E_{SiC} = 400$  GPa,  $\nu_{Al} = 0.33$ ,  $\nu_{SiC} = 0.20$ ,  $\sigma_Y$  (6061-T6) = 0.400 GPa,  $d\sigma/d\varepsilon_m^{pl}$  (6061-T6) = 8.0 GPa.

Due the alignment of the particles, axial modulus and yield strength is predicted to be higher than transverse modulus and yield strength. Both properties increase with increasing reinforcement volume fraction due to enhanced load-sharing. For

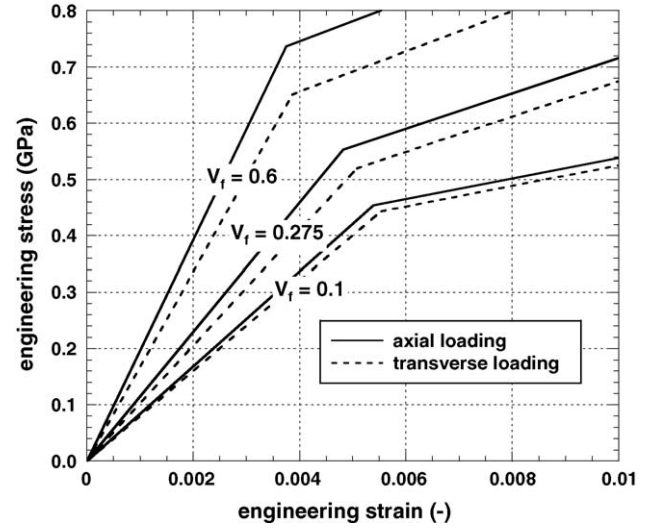


Fig. 3. Composite axial and transverse tensile responses, as predicted by Eshelby model for reinforcement volume fractions of 0.1 and 0.6. Also shown are predicted stress–strain responses in the axial and transverse loading directions for a composite with overall volume fraction of 0.275, corresponding to the (hypothetical) homogeneous composite material, Al-6061/SiC/27.5p.

volume fractions less than 0.5, the *initial* strain-hardening rate,  $d\sigma/d\varepsilon_c^{pl}$  increases with increasing volume fraction as load-sharing becomes more effective whilst for volume fractions greater than 0.5,  $d\sigma/d\varepsilon_c^{pl}$  decreases due to the decreasing volume fraction of matrix. The Eshelby model therefore predicts the maximum strain-hardening response at  $V_f = 0.5$ . The curve for  $V_f = 0.275$  corresponds to the Eshelby prediction for a hypothetical “homogeneous” composite with the same overall volume fraction as the average area fraction measured in the actual composite microstructures,  $A_f = 0.275$ . Although it is not a rigorous upper bound, the “homogeneous” material represents a practical upper limit for composite mechanical properties, since microstructural heterogeneity has a negative effect on mechanical properties in these materials.

#### 4.2. Microstructural modeling using finite elements

Since the Eshelby approach provides no spatial information for modeling, a finite element scheme was developed to combine the spatial information contained in the microstructural images with the constitutive responses of the individual elements predicted by Eshelby. Each element is modeled as a microstructural domain consisting of a uniform spatial distribution of ellipsoidal reinforcement particles, at a particular volume (area) fraction calculated from the individual pixel gray-levels in the corresponding digital micrograph. A custom pre-processor was developed in order to correctly assign the 256 different material property definitions used in the finite element code, corresponding to the 256 available gray-levels in the image. Although this is an approximation of the true microstructural details at the micromechanical length scale, the assumption of a uniform distribution of reinforcement inside each element enables the model to extend over a large area of microstructure without requiring a prohibitively large number of elements.

Each of the models presented in this work covers an area of  $667 \mu\text{m} \times 667 \mu\text{m}$ , corresponding to 16,384 microstructural domains (finite elements) in a  $128 \times 128$  square mesh. The level of discretization was chosen for computational expediency, with the size of each element being much smaller than the homogeneous length scale. Each  $667 \mu\text{m} \times 667 \mu\text{m}$  model is estimated to contain at least 1000 particles, by stereological analysis. It was anticipated that there would be significant amounts of scatter in the predicted stress–strain curves from the FEM, owing to the microstructural variability inherent in the composite materials. A full 3D solution was therefore considered (rather than a 2D plane-stress, plane-strain or axisymmetric solution) in order to provide more precise results. The 3D solution can also be easily extended to multiple layers, for example to model 3D microstructural data obtained via automated serial-sectioning or computed X-ray tomography techniques, as these datasets become more readily available [41]. Eight-noded linear 3D brick elements (C3D8) with equal side lengths were chosen throughout, with no variation of properties with depth. During axial and transverse loading, one side of the mesh is subjected to a uniform displacement in the loading direction, with the opposite side of the mesh constrained for zero displacement along the same direction. In addition, one corner of this constrained side is further constrained in all degrees of freedom to prevent rigid-body motion of the mesh. The analysis was carried out using ABAQUS/Standard (version 6.4-3) on a single-processor machine, with total run-times less than 1 h, providing elastic-plastic solutions for 10 separate strain steps up to a total strain of 1.0%.

#### 4.2.1. Validation of FEM method

In order to validate the FEM method outlined above, an attempt was made to compare output from the model with previously published [23,42] experimental stress–strain data for an extruded Al-2080/SiC/30p-T6 DRA material, of similar microstructure to the present DRA. Optical micrographs were obtained from the authors, showing longitudinal sections through the material. A  $507 \mu\text{m} \times 347 \mu\text{m}$  region of the DRA microstructure, containing the axial and transverse directions was selected, digitized, binarized (thresholded) and resampled to provide a  $95 \times 65$  rectangular grid of square finite elements. As before, each element was given properties according to its volume fraction (gray level) following the Eshelby treatment. The matrix and reinforcement constituent properties used for the model were based on Chawla's original measurements:  $E_{\text{Al}} = 74 \text{ GPa}$ ,  $E_{\text{SiC}} = 410 \text{ GPa}$ ,  $\nu_{\text{Al}} = 0.33$ ,  $\nu_{\text{SiC}} = 0.19$ ,  $\sigma_Y$  (2080-T6) =  $0.390 \text{ GPa}$ ,  $d\sigma/d\varepsilon_m^{\text{pl}}$  (2080-T6) =  $10.8 \text{ GPa}$ ,  $s = 2.00$ .

Fig. 4 shows there is fairly good agreement between the experimental stress–strain behavior of the Al-2080/SiC/30p material and the prediction from the combined Eshelby-FEM technique. The elastic portion of the curve is very well matched, and the strain-hardening rate is similar over quite a broad range of total strain, up to  $\sim 1.2\%$ . Clearly, as strain increases beyond this, the assumption of linear work-hardening in the matrix becomes less appropriate, since localized damage may be occurring in the experimental material which is not addressed in the

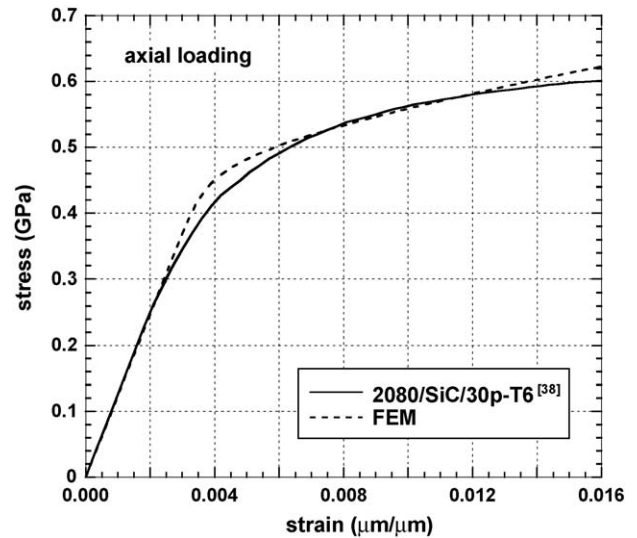


Fig. 4. Comparison between experimentally-generated [42] stress–strain curve for extruded Al-2080/SiC/30p-T6 DRA material and results from combined Eshelby-FEM (axial loading).

present model. However, the model appears appropriate for low strains (i.e. less than 1%). There is also a significant difference in the two curves in the region around the yield point, with the yield strength of the model being higher than in the experiment. This is most likely due to volume-averaging of the matrix stresses in the present model which will tend to overestimate the stress necessary to cause yielding [33]. Additional complications may arise due to thermal residual stresses from processing the DRA. Although micro-yielding phenomena are not explicitly addressed in the present model, their effect and the associated influence of thermal residual stresses will be investigated in a future publication.

## 5. Results

### 5.1. Quantification of spatial homogeneity in anisotropic microstructures

The anisotropic MSAF procedure was used to analyze a total of 15 separate digital images, corresponding to five different  $667 \mu\text{m} \times 667 \mu\text{m}$  regions of interest (ROI's) in each of the three different extruded DRA microstructures. Fig. 5 shows the axial and transverse variations of  $CV(A_f)$  for each material, as a function of strip length,  $Q$ , averaged over the five different ROI's. The plots also show least-squares curve fits to the data, using Eq. (14), where  $\alpha$  is a geometric factor related to the mean particle size ( $d_p$ ) and the mean area fraction ( $A_f$ ) and  $\xi$  is the slope of the straight-line portion on the log–log plot

$$CV(A_f) = \left[ \left( \frac{A_f}{1 - A_f} \right) + \alpha Q^{-2\xi} \right]^{-0.5} \quad (14)$$

The anisotropic homogeneous length scales,  $L_{H1}^{0.1}$  and  $L_{H2}^{0.1}$  are plotted as inverted triangles on the horizontal axis. These are obtained by extrapolating the least-squares curve fits from Eq. (14) to  $CV(A_f) = 0.1$ . There is a steady decrease in spatial homo-



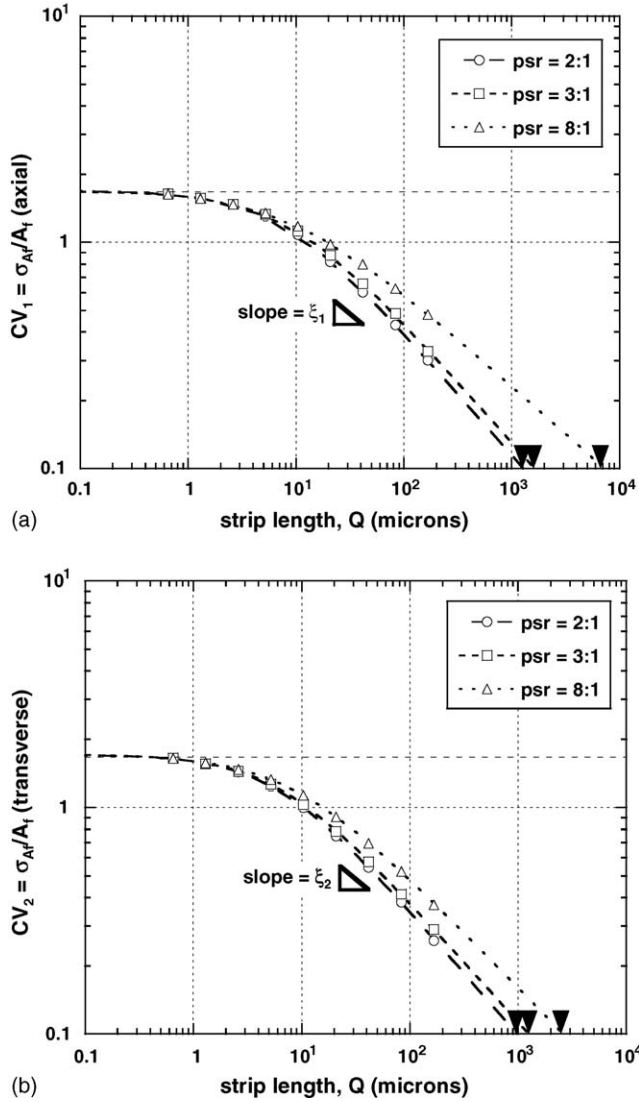


Fig. 5. Anisotropic MSAF results for extruded DRA microstructures in: (a) axial, and (b) transverse directions. The inverted triangles on the horizontal axis are the in-plane homogeneous length scales,  $L_{H1}^{0.1}$  and  $L_{H2}^{0.1}$ . Not only is there a decrease in spatial homogeneity with increasing PSR, the spatial homogeneity for each DRA microstructure is lower in the extrusion direction than in the transverse direction due to microstructural anisotropy introduced by the extrusion process. In addition, the slopes of the linear portions on the plots rank approximately with increasing PSR, indicating decreasing spatial homogeneity.

ogeneity with increasing PSR, as characterized by increases in both anisotropic homogeneous length scales,  $L_{H1}^{0.1}$  and  $L_{H2}^{0.1}$ . Furthermore, at each PSR, the spatial homogeneity is lower in the extrusion direction than in the transverse direction due to microstructural anisotropy introduced by the extrusion process. The ratio  $L_{H1}/L_{H2}$  can be used as an indication of the amount of anisotropy in the microstructure, and is typically found to increase with increasing PSR.

Additional evidence for decreasing spatial homogeneity with increasing PSR is provided by the slopes of the linear portions on the plots ranking approximately with increasing PSR. This is easily understood, since over all length scales there will be higher values of  $CV(A_f)$  as the microstructural variability increases. However, the measured slopes are generally a less-sensitive mea-

Table 1

Anisotropic microstructural descriptors for each extruded DRA microstructure

Particle size ratio	$L_{H1}^{0.1}$ (μm)	$\xi_1$	$L_{H2}^{0.1}$ (μm)	$\xi_2$
2:1	1250	−0.545	950	−0.558
3:1	1590	−0.535	1250	−0.531
8:1	6650	−0.426	2470	−0.495

sure of spatial homogeneity than the change in homogeneous length scale, and they are more prone to experimental scatter. The averaged values for  $L_{H1}$ ,  $L_{H2}$ , and  $\xi$  are presented in Table 1.

A large number of different microstructural descriptors for homogeneity have been previously presented in the literature. These include descriptors based on Dirichlet and other tessellations [3,6,43–46], inter-particle spacings [5,8,47], radial distribution functions [48],  $n$ -point correlation functions [28,49,50], skeletonization techniques [51] and measurements of local area fractions [1,29,52–54]. In order to develop the phenomeno-

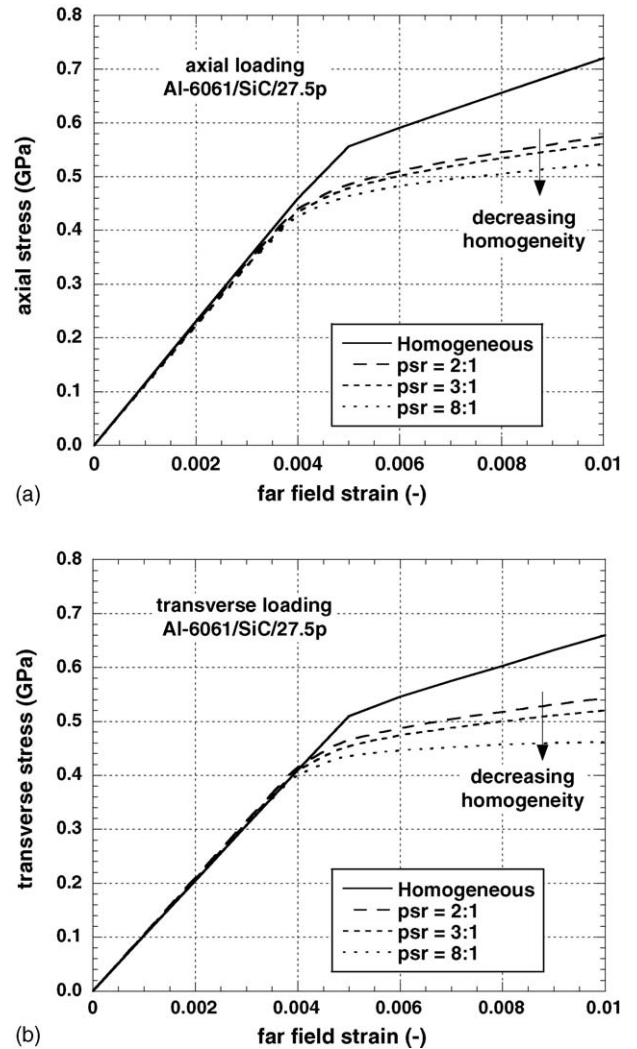


Fig. 6. Typical tensile stress–strain curves for: (a) axial loading, and (b) transverse loading of finite element models of each of the different classes of extruded composites and homogeneous model microstructures. Although the elastic loading portions are similar, the effect of microstructure is evident in the plastic behavior of each material.

logical models necessary for making the first steps towards understanding the complex relationships between microstructure and mechanical behavior, it is important to establish which microstructural descriptors are most relevant. The homogeneous length scales  $L_{H1}$  and  $L_{H2}$  which result from the anisotropic MSAAF analyses are offered as potentially-useful additional microstructural descriptors which capture both homogeneity and anisotropy information in a quantitative way.

### 5.2. Effect of spatial homogeneity on composite tensile stress–strain curves

Fig. 6 shows the axial and transverse tensile stress–strain curves generated from the finite element models, for each of the different classes of extruded composite. Each curve represents tensile data plotted from the model which gave results closest to the average response for all the models in that class. Also plotted are data from homogeneous composite models, containing elements with only one material definition. The homogeneous models represent ideal microstructures, with perfectly uniform packing of aligned ( $s = 2.0$ ) particles at a reinforcement volume fraction of 0.275.

These data show that axial loading produces a higher composite stiffness and a higher yield strength ( $E_1 = 115$  GPa,  $\sigma_{Y1} = 0.558$  GPa) than in the transverse orientation ( $E_2 = 103$  GPa,  $\sigma_{Y2} = 0.519$  GPa), as discussed in Section 4. This is primarily due to the anisotropic material properties that ensue from using non-spherical (i.e.  $s = 2$ ) particles in the Eshelby model, demonstrating that regardless of any possible additional microstructural effects (e.g. due to extrusion), there is still the potential to produce anisotropic mechanical behavior in such a composite. From the elastic portion of the curves, there is very little evidence of any effect of microstructure on the elastic modulus of these composites, since the curves lie almost exactly on top of each other up to the point of yielding. There is, however, a general trend for the post-yield stress–strain curves of the more homogeneous material (i.e. PSR = 2:1) to lie above those for the less homogeneous materials, PSR = 3:1 and PSR = 8:1, in either orientation. The FEM results suggest that decreasing the spatial homogeneity of the microstructure has a significant effect on the predicted stress–strain response, lowering both the yield strength and the subsequent strain-hardening rate.

### 5.3. Influence of spatial homogeneity on elastic behavior

Table 2 provides a summary of the FEM results for the elastic moduli of the different composite microstructures, along with the predictions from the Eshelby treatment. Although there is

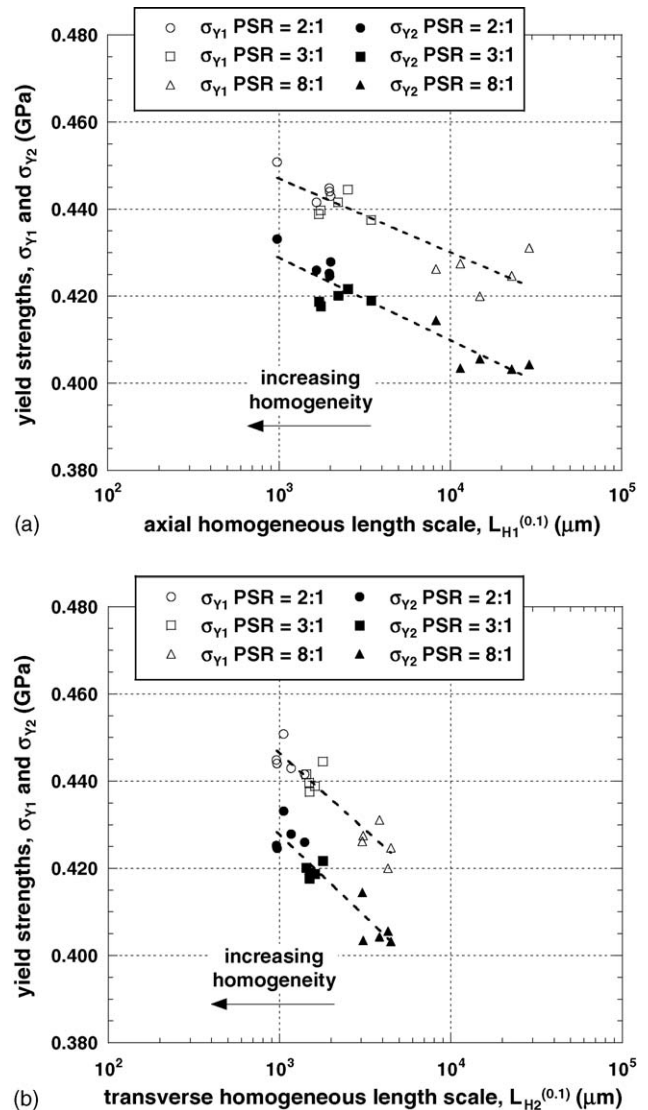


Fig. 7. Finite element results for: (a) axial, and (b) transverse composite yield strengths, plotted vs. the microstructural descriptors  $L_{H1}^{0.1}$  and  $L_{H2}^{0.1}$ . There is a strong effect of decreasing microstructural homogeneity leading to lower yield strengths in each loading direction, with slightly less scatter in the yield strength data plotted vs.  $L_{H2}^{0.1}$ .

a clear difference between the two loading directions due to differences in load-sharing, there is clearly very little influence of microstructural homogeneity on  $E_1$ . There may be a slight decrease in  $E_2$  with increasing PSR, however this is only a very minor effect (i.e. <2% over the whole range of microstructural homogeneities). This constancy of elastic modulus is expected from the results of previous numerical studies of whisker- and particle-reinforced composites using different approaches, where little effect of particle clustering was observed [2,55].

### 5.4. Effect of spatial homogeneity on plastic behavior

In contrast to the relatively minor effect of microstructural homogeneity on the elastic response of the composite models, there is a much stronger influence of microstructure on the plastic behavior. Fig. 7 shows the composite yield strength mea-

Table 2  
Summary of finite element results for axial and transverse elastic moduli

	PSR = 2:1	PSR = 3:1	PSR = 8:1	Homogeneous	Eshelby
$E_1$ (GPa)	113.1	113.0	112.9	116.0	114.7
$E_2$ (GPa)	104.7	104.2	103.1	103.4	102.3

Also shown are data from the Eshelby predictions and finite element results for the “homogeneous” composite models, for comparison.

sured in both the axial and transverse directions plotted versus  $L_{H1}^{0.1}$  and  $L_{H2}^{0.1}$ . Since we are restricting our modeling to the onset of plastic flow (i.e. total strains  $<1\%$ ), we choose as the composite yield strength an offset yield stress corresponding to the flow stress at an overall plastic strain of  $2 \times 10^{-4}$  (i.e.  $\sigma_Y^{0.02\%}$ ). This allows a direct comparison of the different microstructures beyond the micro-yielding regime, but before significant strain-hardening has occurred [56].

There is clearly a much stronger effect of microstructural heterogeneity on the yielding behavior of the composites than is observed for the elastic behavior, for example there is a difference of 20–30 MPa between the yield strengths of the least homogeneous microstructure and the most homogeneous microstructure measured in both the axial and transverse direc-

tions. Also, there is slightly less scatter in the yield strength data when it is plotted versus the transverse homogeneous length scale,  $L_{H2}^{0.1}$ , compared to when it is plotted versus the axial homogeneous length scale,  $L_{H1}^{0.1}$ . This may suggest that this particular microstructural descriptor is slightly more relevant than its counterpart in the axial direction. This observation will be discussed further in the context of strain localization in the inter-cluster regions (see Section 6).

Additional observations regarding the plastic behavior of the composites are presented in Fig. 8 which shows the effect of microstructural homogeneity on the initial strain-hardening response of the different composite microstructures. Also plotted for comparison are data for the strain-hardening rates calculated for the homogeneous composite models and predictions from the Eshelby model. The strain-hardening rate is evaluated at overall strains of between 0.005 and 0.006.

From the figures it is apparent that there is a strong effect of microstructural homogeneity on the initial strain-hardening behavior of the composite microstructures. This effect is clearly stronger than the effect on yield strength, which is in turn much stronger than the effect of microstructural homogeneity on elastic modulus. Furthermore, there is a stronger effect of microstructural homogeneity on the transverse response than the axial response. For example, there is a factor of around 1.4 between the initial strain-hardening rates calculated for the axial direction in the most homogeneous and least homogeneous composite microstructures. This factor more than doubles when comparing the same microstructures in the transverse direction, suggesting a higher sensitivity to microstructural homogeneity in this loading direction. This significant knock-down

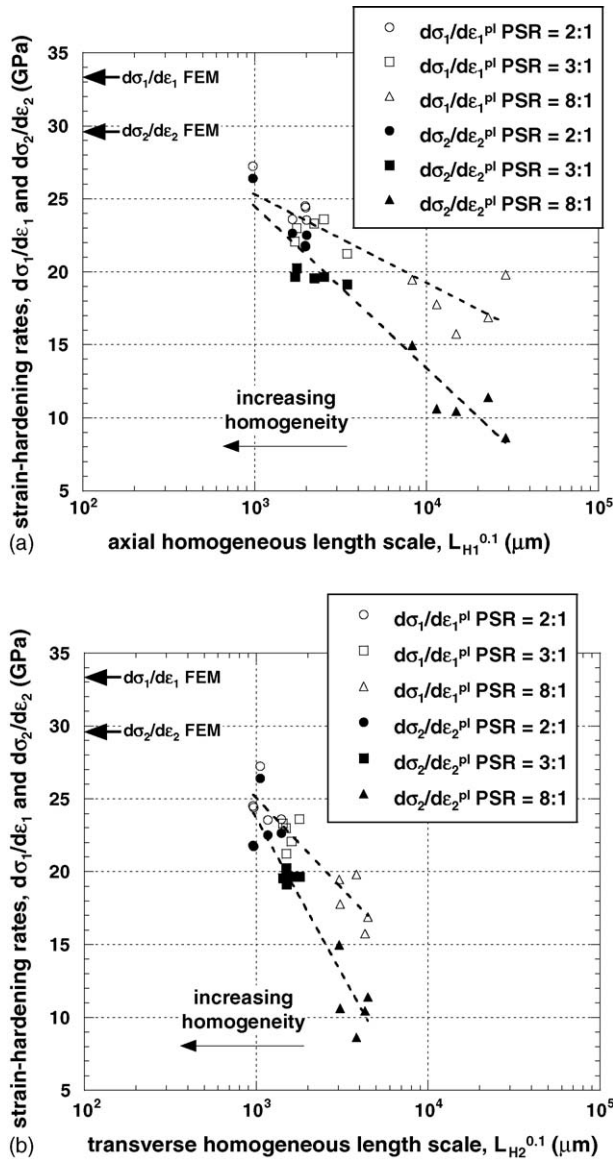


Fig. 8. Finite element results for: (a) axial, and (b) transverse composite strain-hardening rates, plotted vs. the microstructural descriptors  $L_{H1}^{0.1}$  and  $L_{H2}^{0.1}$ . Microstructural homogeneity has a positive effect on the strain-hardening rates evaluated in both loading directions, with a stronger effect being observed for loading in the transverse direction compared with the axial direction.

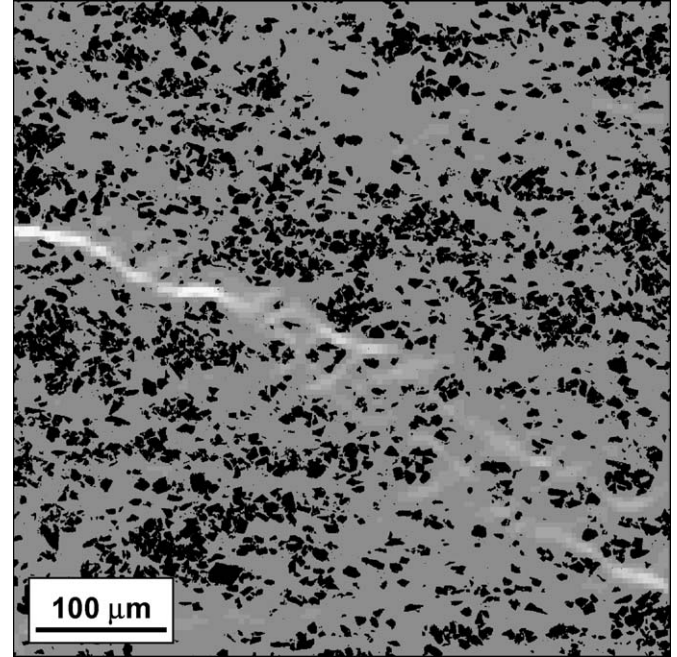


Fig. 9. Contour plot showing regions of high equivalent plastic strain in PSR=8:1 composite microstructure, obtained under transverse loading at a far-field applied stress of 451 MPa for material with PSR=8:1 under transverse loading. The maximum (white) contour corresponds to  $\epsilon_{pl}^{eq} = 0.15$ , loading direction is vertical.



effect on the strain-hardening ability of these composites could have important ramifications in terms of ultimate strengths and the failure mechanisms operating under different conditions of homogeneity.

## 6. Discussion

In order to better understand the role of microstructural homogeneity on determining the plastic behavior of the different composite microstructures, contour plots of stress and strain field quantities were generated from the FEM output files. For example, Fig. 9 shows an elongated band of high equivalent plastic strain in the PSR=8:1 material subject to transverse loading (vertical on the figure). There is intense strain localization, wherein the most intense plastic straining is localized to regions of lower-than-average volume fraction. The existence of these regions is a direct consequence of increasing local variability of reinforcement fraction with increasing microstructural heterogeneity,  $CV(A_f)$ . For a constant average reinforcement fraction, the formation of higher-than-average volume fraction regions (i.e. clusters) necessitates the associated formation of regions of low volume fraction, i.e. the inter-cluster regions. The FEM results suggest that the clusters play a role in controlling deformation, by providing local constraint to the plastically-

deforming regions. For example, the three circled regions in Fig. 10(c) are regions that are experiencing enhanced localized plastic deformation, due to the interactions between the adjacent high volume fraction regions (the clusters) and the applied load, which is horizontal in the figure.

The spatial arrangement of the clusters with respect to the loading axis is therefore important: clusters arranged in pairs parallel to the applied load have a higher propensity for strain localization in the inter-cluster region than those oriented in pairs normal to the applied load. Microstructural anisotropy (i.e. differences between  $L_{H2}^{0.1}$  and  $L_{H1}^{0.1}$ ) can therefore play an important role in controlling the response of these materials. To illustrate this, Fig. 11 shows the data for initial strain-hardening rates measured in each of the microstructures re-plotted versus the homogenous length scale measured perpendicular to the loading axis. In the plot, both the axial and transverse loading data are combined, i.e. for axial loading,  $d\sigma_1/d\varepsilon_1$  is plotted versus  $L_{H2}^{0.1}$  and for transverse loading,  $d\sigma_2/d\varepsilon_2$  is plotted versus  $L_{H1}^{0.1}$ .

The figure reveals a single relationship for both axial and transverse loading, between the initial strain-hardening rate and the homogeneous length scale measured perpendicular to the loading axis. Increasing the microstructural homogeneity in the direction perpendicular to the load results in much higher strain-hardening rates. This effect can be explained by considering the

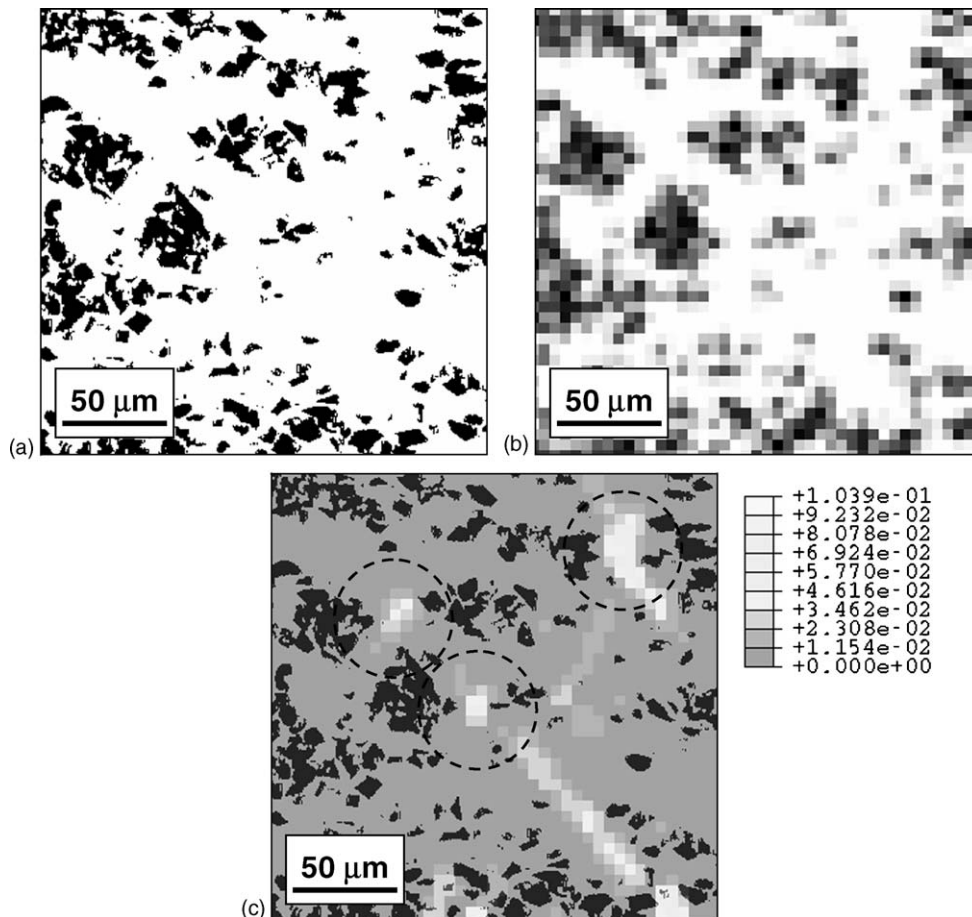


Fig. 10. Indications of plastic strain localization (circled) in PSR = 8:1 microstructure: (a) binary image of particles, (b) finite element mesh of same region, (c) equivalent plastic strain contours. Loading is applied axially (i.e. horizontal) with a far-field stress of 451 MPa.



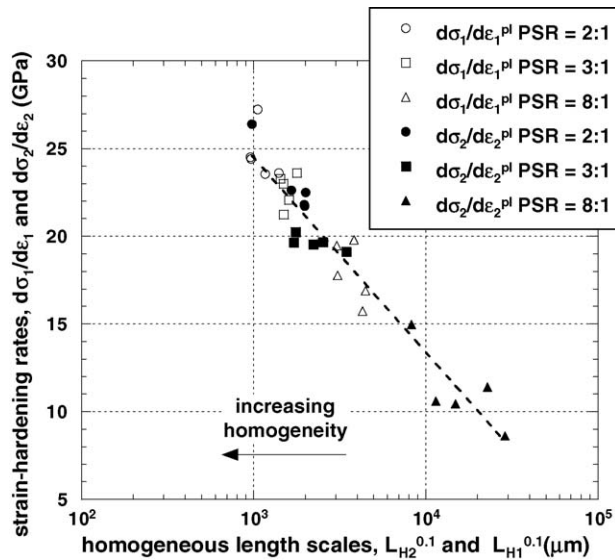


Fig. 11. Plot showing initial strain-hardening rates  $d\sigma_1/d\varepsilon_1$  and  $d\sigma_2/d\varepsilon_2$  re-plotted vs. the homogeneous length scale measured transverse to each loading axis (i.e. compare with Fig. 8(a) and (b)). The strain-hardening data all collapses onto a single line, suggesting that there is a general relationship between the initial strain-hardening rate and the spatial homogeneity of the microstructure, measured perpendicular to the applied load.

influence of microstructural homogeneity on the formation of extended regions of localized plastic strain, analogous to the deformation bands which are familiar in homogeneous materials that exhibit very low work-hardening rates [11]. For example, under axial loading, it is the spatial homogeneity in the transverse direction (i.e.  $L_{H2}$ ) which is the relevant microstructural descriptor. As  $L_{H2}$  increases (i.e. it becomes less homogeneous), the probability for forming extended regions of low reinforcement volume fraction also increases. This, in turn, facilitates strain localization in these regions which leads to a lower overall strain-hardening response in the composite. Similar arguments hold for loading in the transverse direction, with the added caveat that in these composite microstructures, the spatial homogeneity in the axial direction (i.e. perpendicular to the transverse loading axis) is typically lower than in the transverse direction due to microstructural anisotropy imparted via extrusion processing;  $L_{H1} > L_{H2}$ . Consequently, strain-hardening rates measured in the transverse direction should be lower than those measured in the axial direction. This is clearly demonstrated in the strain-hardening data presented here.

In general, there is a significant increase in the amount of strain localization when transverse loading response is compared with the axial loading response. In order to show quantitatively the effect of microstructural homogeneity on the distribution of stresses and strains within the composites, mean equivalent plastic strains were computed. Table 3 shows the mean equivalent plastic strains generated at far-field applied stresses of 451 MPa, for both axial and transverse loading directions. This particular stress level was chosen to reflect the post-yielding behaviors of each microstructure. The table shows that for an applied stresses of 451 MPa in the axial loading direction, there is an increase in plastic strain as microstructural homogeneity decreases. In the

Table 3

Mean values of equivalent plastic strain generated under axial and transverse loading with a far-field applied stress of 451 MPa

	Equivalent plastic strain, $\varepsilon_{pl}^{eq} (\times 10^{-6})$			
	PSR = 2:1	PSR = 3:1	PSR = 8:1	Homogeneous
Axial loading	207	239	437	0 <sup>a</sup>
Transverse loading	301	480	2709	0 <sup>a</sup>

Also included are mean equivalent plastic strains for a “homogeneous” composite with an overall volume fraction of 0.275.

<sup>a</sup> Indicates no yielding.

transverse loading direction, this effect is even more dramatic. The rapidly increasing plastic strain is due to the strain partitioning that is occurring during deformation. For example, Fig. 12 shows that there is a dramatic increase in the amount of plastic

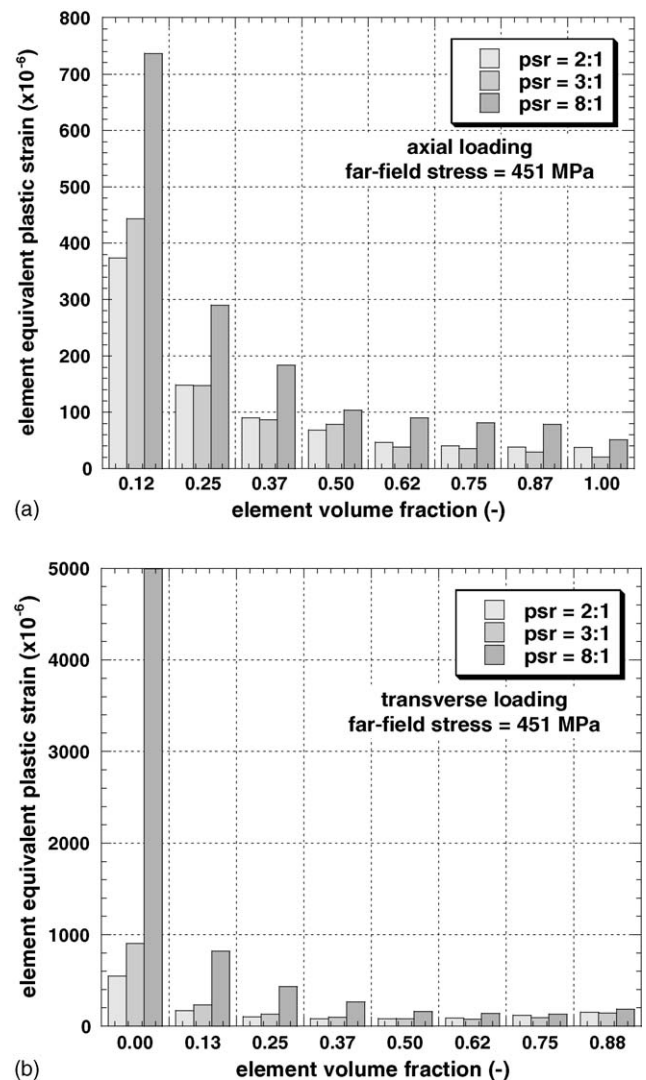


Fig. 12. Histograms showing the distribution of equivalent plastic strain vs. element volume fraction: (a) axial loading, (b) transverse loading. Equivalent plastic strains were generated at a far-field stress of 451 MPa. There is a dramatic increase in plastic strains for elements with lower volume fractions, and this is further enhanced as microstructural homogeneity decreases, due to intense strain partitioning.

strain seen in elements with low volume fractions. Furthermore, there is a clear effect of microstructure, with the least homogeneous material exhibiting the highest levels of plastic strain at the lower volume fractions, due to increased levels of strain partitioning in these materials. The effect is most severe in the case of PSR = 8:1, loaded in the transverse orientation, where  $\varepsilon_{pl}^{eq} \sim 0.005$  for the lowest volume fraction elements, whereas the average  $\varepsilon_{pl}^{eq}$  is only  $\sim 0.00089$  (i.e. an increase of  $5.6\times$ ). At the other end of the scale, the “homogeneous” composite microstructure shows zero plastic strain at this level of applied stress, i.e. the material has not yet yielded.

If these strain localization effects can be extrapolated to much higher strain levels, the relationships between spatial homogeneity and strain localization identified by the present model may also hold implications for the potential failure mechanisms which can operate in these materials. In the case of extremely low spatial homogeneity (e.g. high PSR), the propensity for strain localization is high, and the projected strain-hardening rate is low, therefore, it could be argued that a strain-controlled failure mechanism such as void nucleation and coalescence might occur. Conversely, for more homogeneous composite microstructures wherein strain localization is suppressed, a stress-controlled mechanism such as particle cracking and/or interfacial debonding might operate. In the former case, the strain-hardening behavior of the matrix itself would play an important role in determining the overall failure strain of the composite. Increasing the spatial homogeneity of the composite microstructure is could therefore be considered a potential way to improve the mechanical behavior of the material, by allowing other microstructural enhancements such as stronger particles [57,58] and/or stronger interfacial bonding [59,60] to dominate the mechanical response of the composite, rather than the properties of the matrix.

## 7. Conclusions

The effect of spatial homogeneity on the elastic-plastic mechanical response of extruded Al-6061/SiC/27.5p DRA has been predicted, using a combined approach for microstructural characterization and modeling. Spatial homogeneity is quantified using an extended, anisotropic Multi-Scalar Analysis of Area Fractions procedure, resulting in two microstructural descriptors: the homogeneous length scales,  $L_{H1}$  and  $L_{H2}$ , measured parallel and transverse to the extrusion axis, respectively. A new model for predicting the effect of spatial homogeneity on mechanical behavior was proposed which sought to incorporate a mean-field (Eshelby) micromechanical model within a simple finite element model, thereby dramatically increasing the model's extent without increasing its complexity. This model enables the investigation of deformation mechanisms occurring over length scales encompassing many particle diameters, such as plastic strain localization and deformation banding, without requiring long run-times, by using a volume-averaged, discretized approach. A key assumption in this approach is that below the length scale of the discretization, the microstructure can be modeled by a uniform array of reinforcement parti-

cles. The effect of the level of discretization on predictions of microstructure-property relationships are not addressed directly in the present work, however, detailed comparisons of the present model with discretely-modeled matrix-particle geometries will form the basis of a subsequent publication, to encompass phenomena such as localization of plastic deformation between particles, and subsequent matrix-particle debonding. Nevertheless, empirical models were generated which describe the effect of spatial homogeneity on the elastic and plastic behavior of the composite microstructures. The results confirmed that spatial homogeneity plays only a minor role in elastic deformation, but has a larger effect on the yield strength. By far the strongest effect is on the strain-hardening rate, where the formation of deformation bands is promoted by the more heterogeneous, anisotropic arrangements of the SiC particles. There is a strong directionality to this effect, with the relevant (i.e. controlling) microstructural descriptor identified as the homogeneous length scale measured *perpendicular* to the loading direction. A universal relationship is proposed between the homogeneous length scale measured perpendicular to the loading direction and the strain-hardening rate. It is postulated that the key mechanism controlling strain-hardening behavior is the interruption of the deformation bands which form in elongated low volume fraction regions in-between the SiC clusters. Results from the FEM analysis suggest that as spatial homogeneity decreases, there is a steady increase in the plastic strain in these regions; equivalent plastic strains can reach 5–6 times the average value for the most clustered microstructures, at the chosen level of discretization. This effect is more noticeable for the transverse loading case, due to the anisotropy of the extruded microstructures.

## Acknowledgements

This work was supported in part by the Air Force Research Laboratory, Materials and Manufacturing Directorate, under Air Force Contract Numbers F33615-01-C-5214 and FA8650-04-D-5233. The author would also like to acknowledge Mr. Herbert M. Mullens (UES Inc.) for developing the custom pre-processor used throughout this work. Thanks also go to Dr. Daniel B. Miracle (AFRL/MLLMD), Prof. Donald A. Koss and Mr. Garth B. Wilks (Penn State University) for technical discussions during the preparation of this article, and to Prof. Nikhilesh Chawla (Arizona State University) for providing the 2080/SiC/30p DRA data.

## References

- [1] J.E. Spowart, Z.-Y. Ma, R.S. Mishra, in: K.V. Jata, M. Mahoney, R.S. Mishra (Eds.), *Friction Stir Welding and Processing II*, TMS, Warrendale, PA, 2003, pp. 243–252.
- [2] S.F. Corbin, D.S. Wilkinson, *Acta Metall. Mater.* 42 (1994) 1311–1318.
- [3] A.M. Murphy, S.J. Howard, T.W. Clyne, *Mater. Sci. Technol.* 14 (1998) 959–968.
- [4] A.R. Vaida, J.J. Lewandowski, *Mater. Sci. Eng.* A220 (1996) 85–92.
- [5] S. Tao, J.D. Boyd, *Proceedings of the ASM 1993 Materials Congress*, ASM International, Materials Park, OH, Pittsburgh, PA, 1993, pp. 29–40.
- [6] J.J. Lewandowski, C. Liu, *Mater. Sci. Eng.* A107 (1989) 241–255.
- [7] G. Li, Y. Zhao, S.-S. Pang, *Mat. Sci. Eng.* A271 (1999) 43–52.

- [8] M. Li, S. Ghosh, O. Richmond, H. Weiland, T.N. Rouns, *Mat. Sci. Eng. A256* (1999) 153–173.
- [9] M. Li, S. Ghosh, O. Richmond, H. Weiland, T.N. Rouns, *Mat. Sci. Eng. A266* (1999) 221–240.
- [10] L. Mishnaevsky, M. Dong, S. Honle, S. Schmauder, *Comput. Mater. Sci.* 16 (1999) 133–143.
- [11] A. Borbély, H. Biermann, O. Hartmann, *Mater. Sci. Eng. A313* (2001) 34–45.
- [12] D.S. Wilkinson, E. Maire, J.D. Embury, *Mater. Sci. Eng. (A)* A233 (1997) 145–154.
- [13] J.D. Wolodko, Z. Xia, F. Ellyin, *Mater. Sci. Technol.* 16 (2000) 837–842.
- [14] J.R. Brockenbrough, W.H. Hunt Jr., O. Richmond, *Scripta Mater.* 27 (1992) 385–390.
- [15] H.J. Bohm, A. Eckschlager, W. Han, *Comput. Mater. Sci.* 25 (2002) 42–53.
- [16] W. Wu, K. Sadeghipour, K. Boberick, G. Baran, *Mat. Sci. Eng. A332* (2002) 362–370.
- [17] T. Christman, A. Needleman, S. Nutt, S. Suresh, *Mater. Sci. Eng. A107* (1989) 49–61.
- [18] N. Chawla, V.V. Ganesh, B. Wunsch, *Scripta Mater.* 51 (2004) 161–165.
- [19] V.A. Buryachenko, N.J. Pagano, R.Y. Kim, J.E. Spowart, *Int. J. Sol. Struct.* 40 (2003) 47–72.
- [20] J. Bystrom, *Comp. Part B. Eng.* B34 (2003) 587–592.
- [21] V. Tvergaard, *Acta Metall. Mater.* 38 (1990) 185–194.
- [22] H. Shen, C.J. Lissenden, *Mat. Sci. Eng. A338* (2002) 271–281.
- [23] V.V. Ganesh, N. Chawla, *Mat. Sci. Eng. A391* (2005) 342–353.
- [24] J. Boselli, P.D. Pitcher, P.J. Gregson, I. Sinclair, *Mat. Sci. Eng. A300* (2001) 113–124.
- [25] S. Yang, A.M. Gokhale, Z. Shan, *Acta Mater.* 48 (2000) 2307–2322.
- [26] A. Eckschlager, W. Han, H.J. Bohm, *Comput. Mater. Sci.* 25 (2002) 85–91.
- [27] J. Segurado, C. Gonzales, J. Llorca, *Acta Mater.* 51 (2003) 2355–2369.
- [28] A. Tewari, A.M. Gokhale, J.E. Spowart, D.B. Miracle, *Acta Mater.* 52 (2004) 307–319.
- [29] J.E. Spowart, B. Maruyama, D.B. Miracle, *Mater. Sci. Eng. (A)* A307 (2001) 51–66.
- [30] J.C. Russ, *The Image Processing Tool Kit*, Reindeer Games Inc., 1996–1997.
- [31] J.D. Eshelby, *Proc. Roy. Soc. London, Ser. A* A241 (1957) 376–396.
- [32] J.D. Eshelby, in: I.N. Sneddon, R. Hill (Eds.), *Prog. Solid Mech.*, vol. 2, 1961, pp. 89–140.
- [33] T.W. Clyne, P.J. Withers, *An Introduction to Metal Matrix Composites*, Cambridge University Press, Cambridge, 1993.
- [34] T. Mori, K. Tanaka, *Acta Metall.* 23 (1973) 571–574.
- [35] O.B. Pedersen, *Acta Metall.* 31 (1983) 1795–1808.
- [36] T.W. Clyne, P.J. Withers, in: University of Cambridge, Department of Materials Science and Metallurgy, <http://www.msm.cam.ac.uk/mmc/publications/programs/ESHEL.C.ZIP>.
- [37] A.F. Whitehouse, R.A. Shahani, T.W. Clyne, in: N. Hansen, D.J. Jensen, T. Leffers, H. Lilholt, T. Lorentzen, A.S. Pedersen, O.B. Pedersen, B. Ralph (Eds.), *Metal Matrix Composites: Processing, Microstructure and Properties*, Proceedings of the 12th RISØ International Symposium, RISØ, Roskilde, Denmark, 1991, pp. 741–748.
- [38] M. Taya, T. Mori, *Acta Metall.* 35 (1987) 155–162.
- [39] T. Mori, M. Okabe, T. Mura, *Acta Metall.* 28 (1980) 319–325.
- [40] *Metallic Materials and Elements for Aerospace Vehicle Structures: MIL-HDBK-5H*, in: AFRL/MLSC, Wright-Patterson AFB, OH, 1998.
- [41] J.E. Spowart, in: R. Price et al. (Eds.), *Microscopy and Microanalysis*, vol 2, Supplement 2, Cambridge University Press, 1638CD (on CD-ROM).
- [42] N. Chawla, U. Habel, Y.-L. Shen, C. Andres, J.W. Jones, J.E. Allison, *Metall. Mat. Trans. (A)* 31A (2000) 531–540.
- [43] I.C. Stone, P. Tsakirooulos, *Mater. Sci. Technol.* 11 (1995) 213–221.
- [44] R.K. Everett, A.B. Geltmacher, *Scripta Mater.* 40 (1999) 567–571.
- [45] M. Bertram, H. Wendrock, *J. Microsc.* 181 (1996) 45–53.
- [46] N. Yang, J. Boselli, P.J. Gregson, I. Sinclair, *Mater. Sci. Technol.* 16 (2000) 797–804.
- [47] A. Tewari, M. Dighe, A.M. Gokhale, *Mater. Charact.* 40 (1998) 119–132.
- [48] P. Louis, A.M. Gokhale, *Acta Mater.* 44 (1996) 1519–1528.
- [49] S. Torquato, *Appl. Mech. Rev.* 44 (1991) 37–76.
- [50] R. Pyrz, *Mat. Sci. Eng. A177* (1994) 253–259.
- [51] P. Franciosi, H. Lebaill, *Acta Mater.* 52 (2004) 3161–3172.
- [52] I.C. Stone, P. Tsakirooulos, *Mater. Sci. Technol.* 11 (1995) 222–227.
- [53] B. Lu, S. Torquato, *J. Chem. Phys.* 93 (1990) 3452–3459.
- [54] P. Ganguly, W.J. Poole, *Mater. Sci. Eng. A332* (2002) 301–310.
- [55] T. Christman, A. Needleman, S. Suresh, *Acta Metall. Mater.* 37 (1989) 3029–3050.
- [56] M. Kouzeli, A. Mortensen, *Acta Mater.* 50 (2002) 39–51.
- [57] J.E. Spowart, D.B. Miracle, in: J.J. Lewandowski (Ed.), *Proceedings of the 10th International Congress on Fracture (ICF-10)*, Elsevier, Honolulu, HI, 2001.
- [58] S.G. Song, N. Shi, G.T. Gray III, J.A. Roberts, *Met. Mater. Trans. A* 27A (1996) 3739–3746.
- [59] L.M. Tham, M. Gupta, L. Cheng, *Acta Mater.* 49 (2001) 3243–3253.
- [60] A. Needleman, S.R. Nutt, V. Tvergaard, in: S. Suresh, A. Mortensen, A. Needleman (Eds.), *Fundamentals of Metal Matrix Composites*, Butterworth-Heinemann, 1993, Chapter 13.